Dalton Transactions

ROYAL SOCIETY OF CHEMISTRY

PAPER

View Article Online
View Journal | View Issue

Cite this: *Dalton Trans.*, 2022, **51**, 13636

Investigating the chemical sensitivity of melting in zeolitic imidazolate frameworks†

Alice M. Bumstead, [a] Michael F. Thorne, [a] Adam F. Sapnik, [a] Celia Castillo-Blas, [a] Giulio I. Lampronti [b] and Thomas D. Bennett *[a]

Received 4th July 2022,
Accepted 17th August 2022

DOI: 10.1039/d2dt02142k

rsc.li/dalton

The number of zeolitic imidazolate frameworks (ZIFs) that form melt-quenched glasses remains limited, with most displaying the **cag** network topology. Here, we expand our studies to **zni** topology ZIFs, starting with ZIF-zni [$Zn(Im)_2$] before changing its linker chemistry, by incorporating 2-methylimidazolate and 5-aminobenzimidazolate. ZIF-zni was found to melt and form a glass, with T_m = 576 °C and T_g = 322 °C, although it was not possible to prepare the glass without zinc oxide impurities. The addition of 2-methylimidazolate to the structure gave ZIF-61 [$Zn(Im)_{1.35}(mIm)_{0.65}$], which decomposed without passing through the liquid state. However, incorporating small quantities of 5-aminobenzimidazolate resulted in a ZIF [$Zn(Im)_{1.995}(abIm)_{0.005}$] with a lower melting temperature (T_m = 569 °C) than pure ZIF-zni, and no evidence of zinc oxide growth. This demonstrates the sensitivity of melting behaviour in ZIFs towards linker chemistry, with only a 0.25% variation capable of eliciting a 7 °C change in melting temperature. This study highlights the chemical sensitivity of melting in ZIFs and serves as a promising strategy for tuning their melting behaviour.

Introduction

The field of metal–organic frameworks (MOFs) has expanded to encompass defective, disordered, and amorphous materials, with many studies demonstrating that structural disorder can be utilised to enhance chemical and physical properties.[1–6] For example, amorphous MOFs have already gained interest as potential candidates for trapping iodine and encapsulating bioactive molecules.[7–9] These amorphous MOFs retain the short range order of their parent crystalline frameworks, whilst lacking long range periodicity.[10] This results in the observation of only diffuse scattering by X-ray diffraction.[11,12] The most common methods to prepare amorphous MOFs from crystalline frameworks are: by the application of pressure,[13,14] *via* mechanical-milling,[15,16] and, by melt-quenching.[17,18] This final method results in the formation of melt-quenched MOF glasses (a_gMOFs).[19,20]

a_gMOFs have gained particular interest as the first new category of glass formed in 50 years, with potential applications including molecular encapsulation, ion transportation as well as coating and display technologies.[21–23] A key feature that differentiates a_gMOFs from other amorphous MOFs is that, upon heating, they exhibit a reversible transition known as the glass transition (T_g) where the glass transforms to a more flowable, liquid-like state.[19,24] To successfully prepare a_gMOFs, crystalline MOFs with a stable liquid state prior to their thermal decomposition temperature (T_d) are needed.[20,21] However, currently, the range of crystalline frameworks that fit this criterion are limited.

Zeolitic imidazolate frameworks (ZIFs) are the most common family of MOFs that have been reported to undergo melt-quenching.[20,21] ZIFs are composed of metal ions, often Zn^{2+} or Co^{2+}, tetrahedrally coordinated to imidazolate type linkers.[25–27] Melting in ZIFs has been demonstrated to occur on a picosecond timescale by de-coordination and subsequent re-coordination of the imidazolate linkers.[28,29] ZIFs have a rich topological landscape, with over 300 crystal structures deposited in the CCDC,[30,31] and exhibit rich polymorphism.[32–37] For example, one of the simplest ZIF compositions [$Zn(Im)_2$] (Im – imidazolate – $C_3H_3N_2^-$) has been reported to crystallise with more than 10 different network topologies.[32,38]

However, the number of ZIFs that exhibit a stable liquid state—and are thus suitable candidates for glass formation—remain scarce. In fact, most a_gMOFs reported to date have been prepared from crystalline ZIFs displaying the **cag** network topology,[17,18] with different linker chemistries,[39,40] and metal ions,[41,42] incorporated to alter their thermal response. The most well-studied of these systems is ZIF-62 [$Zn(Im)_{2-x}(bIm)_x$]

[a]*Department of Materials Science and Metallurgy, University of Cambridge, Cambridge, CB3 0FS, UK. E-mail: tdb35@cam.ac.uk*
[b]*Department of Earth Sciences, University of Cambridge, Cambridge, CB2 3EQ, UK*
† Electronic supplementary information (ESI) available. See DOI: https://doi.org/10.1039/d2dt02142k

(bIm – benzimidazolate – $C_7H_5N_2^-$), with T_m = 437 °C and T_g = 318 °C when x = 0.25,[17] and the possibility to further tune these values by altering the value of x.[18,19]

This apparent scarcity in melting ZIF topologies has been rationalised by first principles molecular dynamics simulations.[29] They revealed that dense networks favour melting, due to the greater number of dispersive interactions available to stabilise uncoordinated linkers during the melting process. This has been supported by experimental studies which have demonstrated that ZIFs displaying more open networks such as ZIF-8 (SOD topology, ρ = 1.14 g cm^{-3}) and ZIF-76 (LTA topology, ρ = 0.99 g cm^{-3}) do not have a stable liquid state prior to decomposition.[28,39]

One of the densest ZIFs reported to date is ZIF-zni (ρ = 1.56 g cm^{-3}), a ZIF with the [Zn(Im)$_2$] composition, crystallising in a tetragonal unit cell with the $I4_1cd$ space group and exhibiting the **zni** topology (Fig. 1).[32,43,44] First reported in the 1980s, before the widespread study of MOFs and ZIFs, modelling has demonstrated it to be one of the lowest energy ZIF structures.[32,36,43,45] It is also reported to exhibit structural changes under the influence of external stimuli. For example, it was demonstrated that, under hydrostatic pressures between 0.5–0.8 GPa, ZIF-zni undergoes an irreversible phase transition *via* complex bond rearrangement, predominantly along the *ab* plane, to a lower symmetry ($I4_1$) polymorph denoted ZIF-coi.[46,47] The close relationship between these polymorphs was then confirmed when it was reported that ZIF-coi undergoes an irreversible phase transition to ZIF-zni when heated to temperatures above 360 °C.[38,47,48]

ZIF-zni has also been demonstrated to be an important intermediate in the melting process of certain ZIFs such as **cag** topology ZIF-4 [Zn(Im)$_2$]. Heating ZIF-4 revealed a complex thermal response. Thermal amorphisation occurred at 320 °C. This was followed by recrystallisation to ZIF-zni at 400 °C, before this ZIF underwent melting at *ca.* 590 °C.[17] ZIF-zni has also recently been reported to undergo melting at 585 °C when heated directly from room temperature.[44] However, in this study, a T_g was not reported and it was noted that the resulting glass, denoted a_gZIF-zni, contained zinc oxide.[44]

Here, we investigate the thermal response of ZIF-zni in detail to (i) locate its T_g and, (ii) determine whether a_gZIF-zni can be prepared without zinc oxide growth. We then go on to study how the incorporation of different linker chemistry influences melting in **zni** topology frameworks. Incorporation of 2-methylimidazolate (mIm – $C_4H_5N_2^-$) into the structure of ZIF-zni results in the formation of ZIF-61 (Fig. 1), whose thermal behaviour has yet to be reported. Incorporation of 0.25% 5-aminobenzimidazolate (abIm – $C_7H_6N_3^-$) in ZIF-zni, results in an amine-functionalised version—denoted ZIF-zni-NH$_2$ (Fig. 1). Studying the thermal response of this framework allows the sensitivity of melting to very subtle changes in chemical composition to be investigated.

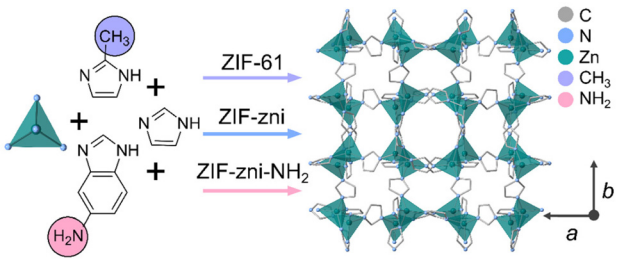

Fig. 1 Schematic of the synthesis of the three **zni** topology ZIFs studied in this work. ZIF-zni is prepared using only imidazole as indicated by the blue arrow. ZIF-61 is synthesised using imidazole and 2-methylimidazole as indicated by the purple arrow. ZIF-zni-NH$_2$ is prepared using imidazole and 5-aminobenzimidazole as indicated by the pink arrow. All three ZIFs display the **zni** topology. The ZIF-zni crystal structure shown is adapted from a published CIF.[46] Atoms and substituents shown: C – grey, N – blue, Zn – green, CH$_3$ – purple and NH$_2$ – pink. Hydrogen atoms are omitted for clarity.

Experimental

Materials

Imidazole (≥99.5%) and D_2O (35 wt% DCl) were purchased from Sigma Aldrich. Dimethyl sulfoxide (DMSO)-d_6 (99.8 atom% D, contains 0.03% (v/v) tetramethylsilane (TMS)) was purchased from VWR. Zinc nitrate hexahydrate (98%) was purchased from Alfa Aesar. *N*,*N*-Dimethylformamide (DMF) (99.5%) and dichloromethane (DCM) (99.8%) were purchased from Fischer Scientific. Zinc oxide (99.5%+), 2-methylimidazole (99%) and *N*,*N*-diethylformamide (DEF) (99%) were purchased from Acros Organics. Acetic acid (99%) was purchased from Chem-Lab. 5-Aminobenzimidazole was purchased from Santa Cruz Biotechnology. All materials were used without further purification.

Characterisation techniques

Powder X-ray diffraction (PXRD)

Data were collected on a Bruker D8 ADVANCE diffractometer equipped with a position sensitive LynxEye detector with Bragg–Brentano parafocusing geometry. Cu Kα radiation (λ = 1.5418 Å) was used. The samples were compacted into 5 mm disks on a low background silicon substrate and rotated during data collection in the 2θ range of 5–40° at ambient temperature. All data conversion from .raw files to .xy files was performed using PowDLL.[49] Pawley refinements were performed using TOPAS-Academic Version 6.[50] Thompson-Cox-Hastings pseudo-Voigt (TCHZ) peak shapes were used along with a simple axial divergence correction. The lattice parameters were refined against the values obtained from the CIF in the 2θ range of 5–40°. The zero-point error was also refined.

Differential scanning calorimetry (DSC)

Data were collected on a Netzsch DSC 214 Polyma Instrument. Heating and cooling rates of 10 °C min^{-1} were used in conjunction with a flowing argon atmosphere. Non-hermetically sealed pans (30 μL) were used. An empty aluminium pan was

used as a reference. Background corrections were performed using the same heating cycle on an empty aluminium crucible. All data analysis was performed using the Netzsch Proteus® software package. T_m was taken as the offset (the end point) of the melting endotherm. T_g was taken as the mid-point of the change in gradient of the heat flow of the DSC on the 2nd upscan.

Thermogravimetric analysis (TGA)

Data were collected on a TA Instruments SDT-Q600 and SDT-Q650 using alumina pans (90 μL). Heating and cooling rates of 10 °C min^{-1} were used, and experiments were conducted under a flowing argon atmosphere. All data analysis was performed using the TA Instruments Universal Analysis software package. The temperature used to define weight changes was determined using the first derivative of the weight (%) trace as a function of temperature.

^{1}H nuclear magnetic resonance (NMR) spectroscopy

^{1}H NMR spectra were recorded at 25 °C using a Bruker AVIII 500 MHz Spectrometer with a dual ^{13}C/^{1}H (DCH) cryoprobe at the Department of Chemistry, University of Cambridge. A solvent mixture of DCl (35%)/D_2O and DMSO-d_6 in a 1 : 5 ratio with tetramethylsilane (TMS) as a reference was used for all samples. All data processing was performed using TopSpin 4.0.7.

Variable temperature powder X-ray diffraction (VTPXRD)

Bulk powder samples of ZIF-zni and ZIF-61 were mixed with *ca.* 10% by volume silicon powder, with silicon used as a diffraction standard. Each sample (*ca.* 100 mg) was placed in an alumina sample holder. Diffraction data were then collected under vacuum (8.5×10^{-3} mbar) using a Bruker D8 Advance diffractometer with an MRI high-temperature chamber and a Vantec detector. Cu Kα radiation (λ = 1.5418 Å) was used throughout. The sample height was adjusted before each experiment to optimise the intensity of the silicon standard (111) reflection at *ca.* 28.45° 2θ. Diffraction data sets for both ZIFs were collected at 20 °C intervals from 30 °C up to 450 °C in the 2θ range of 5–40°. Rietveld refinements were performed on the ZIF-zni data series using TOPAS-Academic Version 6.[50] Previously reported silicon thermal expansion data were used to calculate the unit cell parameters for silicon at each temperature.[51] These parameters were then used to correct the peak positions for sample displacement at each temperature. A Pearson VII function was used to model peak shape whilst an 8th order Chebychev polynomial was used to model the background. The lattice parameters were refined against the values obtained from the reported CIF for ZIF-zni in the 2θ range of 5–40°.[46] The scale factor and 8th order spherical harmonics corrections for preferred orientation were also refined. The atomic positions of ZIF-zni were included but were constrained during the refinements. The VTPXRD data were refined sequentially, with the final values obtained from the previous refinement used as the initial values for the subsequent refinement.

Scanning electron microscopy (SEM)

SEM images were collected with a high-resolution scanning electron microscope FEI Nova Nano SEM 450, using an accelerating voltage of 15 kV. All samples were dispersed onto double sided adhesive conductive carbon tape that was attached to a flat aluminium sample holder and coated with a platinum layer (15 nm).

Synthetic methods

ZIF-zni synthesis

Imidazole (8.54 g, 0.125 mol) was added to a solution of zinc oxide (5.00 g, 0.061 mol) dissolved in a 0.5 wt% solution of acetic acid in deionised water (50 ml). This solution was then heated under reflux for 20 min, resulting in the formation of a powdery white precipitate which was collected by vacuum filtration and washed with fresh deionised water. The powder was then soaked in dichloromethane (DCM) (5 ml) overnight before being activated by heating for 3 h at 170 °C under dynamic vacuum. This was based on a reported procedure.[52]

ZIF-61 synthesis

Solutions of imidazole dissolved in *N*,*N*-dimethylformamide (DMF) (0.15 M, 13.5×10^{-4} mol, 9 ml) and 2-methylimidazole dissolved in DMF (0.15 M, 13.5×10^{-4} mol, 9 ml) were mixed together before a zinc nitrate hexahydrate solution in DMF (0.15 M, 6.75×10^{-4} mol, 4.5 ml) was added. The mixture was then heated in an oven at 130 °C and allowed to react solvothermally for 48 h, resulting in the formation of a yellow polycrystalline powder which was collected by vacuum filtration and washed with fresh DMF. This was then soaked in DCM (5 ml) overnight before being activated for 3 h at 170 °C under dynamic vacuum. It should be noted that multiple reactions were attempted, and it was found that heating to temperatures of 130–150 °C for 48–96 h all led to the formation of phase pure crystalline ZIF-61 powder.

ZIF-zni-NH_2 synthesis

Zinc nitrate hexahydrate (0.095 g, 0.50 mmol), imidazole (0.46 g, 6.76 mmol) and 5-aminobenzimidazole (0.10 g, 0.75 mmol) were dissolved in *N*,*N*-diethylformamide (DEF) (4.7 ml). The dark red coloured reaction solution was then heated in an oven at 130 °C and allowed to react solvothermally for 48 h, resulting in the formation of red coloured rod-shaped crystals which were collected by vacuum filtration and washed with fresh DEF. The crystals were soaked in DCM (5 ml) overnight before being activated by heating for 3 h at 170 °C under dynamic vacuum.

Results and discussion

Synthesis and thermal response of ZIF-zni

There are many synthetic procedures available for ZIF-zni, since it was first reported in 1980.[43] However, many result in

the formation of mixed phase materials or low yields of single crystals.[46,53] Here, an acid-catalysed synthesis of ZIF-zni was chosen due to its scalability and high yield (Fig. S1†).[52] Briefly, imidazole and zinc oxide were heated under reflux in a dilute acetic acid solution (0.5 wt%) for 20 minutes, yielding white needle-shaped crystals (Fig. S2 and S3†). Their purity and crystallinity were then confirmed by PXRD (Fig. S4, Table S1†).

The thermal behaviour of ZIF-zni was investigated by TGA and DSC (Fig. 2, S5 and S6†). Less than 1% mass loss occurred below 400 °C suggesting that ZIF-zni was stable up to this temperature and that minimal solvent was left in the pores after activation (Fig. S5†). Thermal decomposition of ZIF-zni was split into several mass loss events starting at 470 °C with *ca.* 5% mass lost in the first decomposition step between 470 °C and 578 °C (Fig. S5†). Assessment of the 1st upscan of the heat flow trace revealed two interesting features upon heating: a small endothermic peak (361 °C, 1.9 J g^{-1}) followed by a sharp endotherm attributed to a melting event (T_m = 576 °C) (Fig. 2 and S6†). These features agree closely with those recently reported for ZIF-zni (*cf.* 357 °C for the small endotherm and 585 °C for the melting event).[44] The melting event for ZIF-zni occurred after the first decomposition step in the TGA trace and so was accompanied by *ca.* 6% mass loss (Fig. S5†). Upon reheating, a T_g = 322 °C (Fig. 2 and S6†) was observed, suggesting that thermal decomposition was not sufficient to prevent glass formation. Our results here differ to previous studies, which did not report a T_g for a_gZIF-zni.[44]

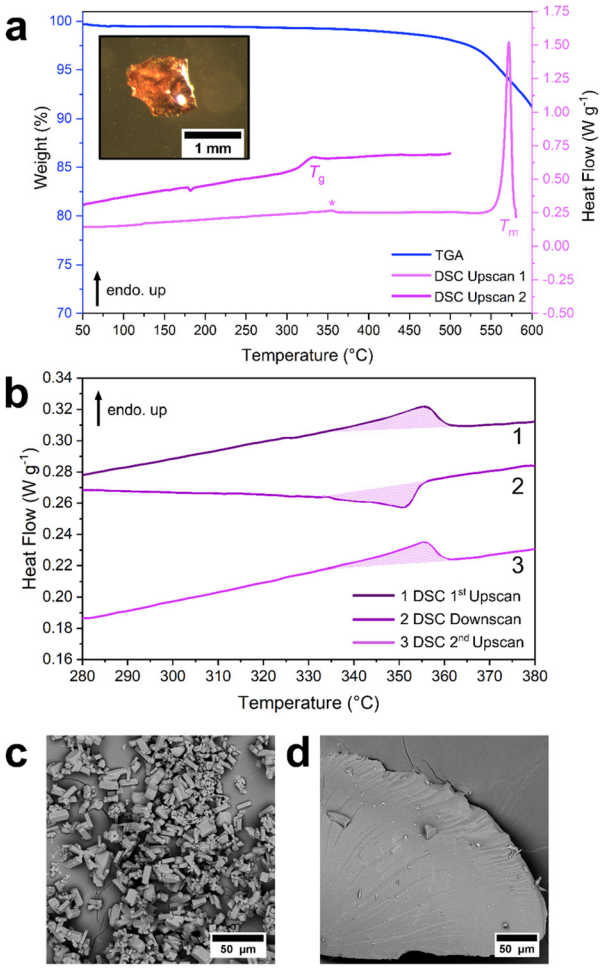

Fig. 2 (a) TGA trace (blue) and DSC traces (purple) of ZIF-zni revealing T_m = 576 °C (1st upscan) when heated to 580 °C and T_g = 322 °C (2nd upscan) when reheated to 500 °C, both measured at 10 °C min^{-1} under argon. The endotherm at 361 °C in the 1st upscan is marked by an asterisk. Inset: image of a fragment of a_gZIF-zni. (b) DSC traces (purple) of ZIF-zni when heated to 400 °C, cooled to 30 °C, then reheated to 400 °C (all measured at 10 °C min^{-1} under argon) demonstrating that the event at 361 °C is reversible on temperature cycling. All DSC scans are offset on the y axis for clarity. SEM images of ZIF-zni (c) and a_gZIF-zni (d), both scale bars are 50 µm.

A sample of ZIF-zni cooled from 580 °C, *i.e.*, from above the melting temperature, exhibited diffuse scattering by PXRD (Fig. S7†), whilst clear evidence of vitreous flow was evident from SEM (Fig. 2, Fig. S8 and S9†), further supporting glass formation. However, the presence of zinc oxide reflections in the diffraction pattern highlight that decomposition accompanied melting (Fig. S7†). This aligns with previous reports of a_gZIF-zni which were also found to contain zinc oxide contamination.[44]

To investigate if it was possible to induce melting in ZIF-zni without the growth of zinc oxide in the framework, a sample of ZIF-zni was heated sequentially to 550 °C, 560 °C, 570 °C, 580 °C, 590 °C and 600 °C followed by *ex situ* PXRD (Fig. S10†). Reflections corresponding to ZIF-zni were observed at temperatures up to 570 °C, suggesting that melting had not finished at this stage, in line with the results from DSC (Fig. S6†). Additionally, evidence of zinc oxide in the structure was seen as low as 560 °C. Above 580 °C, all reflections corresponding to ZIF-zni were lost, and zinc oxide was evident in the amorphous material (Fig. S10†). In the case of ZIF-zni, T_m appears to be too high for melting to occur without some decomposition to zinc oxide.

Discussion of the thermal response of ZIF-zni

The melting temperature observed for ZIF-zni (T_m = 576 °C) is much higher compared to other melting ZIFs such as ZIF-62 (T_m = 437 °C). This is attributed to the higher crystallographic density of the **zni** topology framework (ρ = 1.56 g cm^{-3}) than the **cag** topology framework of ZIF-62 (ρ = 1.29 g cm^{-3}).[44,46,54] A recent first principles molecular dynamics study predicted that melting in **zni** topology frameworks would occur at higher temperatures than **cag** topology systems and this was attributed to the higher density of the **zni** framework hindering the extent of linker dissociation possible during melting.[29]

The T_g of ZIF-zni (322 °C) was found to be higher than that reported for ZIF-4 (T_g = 292 °C),[25,44] despite these frameworks having the same composition [Zn(Im)$_2$].[17] The densities of these glasses have been found to be extremely similar (*cf.* 1.37 g cm^{-3} for a_gZIF-zni and 1.38 g cm^{-3} for a_gZIF-4).[44] Therefore, it is unlikely that this contributes to the difference in T_g observed. One possible cause for this difference in T_g may be the difference in thermal history between the two glasses. It seems that a complex interplay of thermal history,

framework density and topology all influence melting and glass formation in ZIFs.

Further investigating the thermal response of ZIF-zni

To further understand the thermal behaviour of ZIF-zni, the endotherm at 361 °C in the DSC was investigated. ZIF-zni was heated to 400 °C (*i.e.*, above the feature of interest), cooled to 30 °C, then re-heated to 400 °C (Fig. 2, S11, S12†). The feature was seen in both heating and cooling scans with very similar enthalpy changes, suggesting a reversible event (Fig. 2, S11 and S12†). In previous studies, it was proposed that the bulk powder sample of ZIF-zni was impure and that it contained a small quantity of the closely related ZIF-coi polymorph as an impurity.[44] This endotherm was then attributed to the **coi** phase impurity transitioning to the bulk **zni** phase.[44] However, the phase change between **coi** and **zni** is reported to be irreversible,[44,47] so this assignment is not in agreement with our findings here. Furthermore, no discernible changes in the diffraction pattern were observed after holding ZIF-zni at 365 °C for 1 hour (Fig. S13†).

To further investigate the feature observed at 361 °C, an *in situ* VTPXRD study was performed (Fig. 3, S14–17,† Tables S2–4†). VTPXRD data were collected at 20 °C intervals from 30 °C up to 450 °C. The diffraction patterns were found to be relatively unchanged throughout heating (Fig. 3, Fig. S14 and S15†). A drop in peak intensity was seen at higher temperatures. This is attributed to a loss in crystallinity as the sample was held at elevated temperatures for an extended period during data collection. This was accompanied by very subtle changes in the peak positions of certain reflections, in accordance with their lattice parameter dependence (Fig. S15†). The VTPXRD data collected here suggest that ZIF-zni does not undergo a crystallographic phase change upon heating, and that the feature observed at 361 °C is likely due to a more subtle structural change.

The VTPXRD patterns were then examined in more detail, specifically focussing on changes in the lattice parameters and the overall unit cell volume. Below 400 °C, an approximately linear increase in the *a* lattice parameter with temperature was observed along with an increase in the unit cell volume by 1.5% (Fig. 3 and S15†). This was accompanied by a decrease in the *c* lattice parameter. Interestingly, at 410 °C, the unit cell volume decreased by 0.25%. Consequently, both the *a* and *c* lattice parameters decreased at this temperature. This occurs at a similar temperature to the endothermic feature observed in the DSC trace, suggesting these events may be related. Above 410 °C, the unit cell volume and lattice parameters increased in value.

Previous studies used molecular dynamics simulations to probe the structure of ZIF-zni at 377 °C.[47] Trigonal coordination environments were predicted to form at this temperature as an imidazolate linker was expelled from the coordination sphere of the zinc centre.[47] It was predicted that both lattice parameters contract in response to the formation of these trigonal centres, resulting in a reduction in the overall unit cell volume.[47] This hypothesis was then corroborated by evidence of a unit cell volume contraction of *ca.* 1% by X-ray diffraction at this temperature.[47] We therefore speculate that similar behaviour is responsible for the unit cell contraction observed here. The endotherm seen in the DSC further supports this hypothesis as energy would be required to break the Zn-N bonds to form the proposed trigonal centres in the contracted unit cell.

These proposed trigonal centres in ZIF-zni are highly similar to those predicted to form during the melting process in ZIFs.[28,29] Moreover, many ZIFs have been reported to undergo thermal amorphisation before recrystallising to ZIF-zni at *ca.* 400 °C, with these events proposed to occur *via* a change in framework connectivity.[55] We therefore speculate that linker de-coordination and formation of trigonal zinc centres in ZIFs contributes to many thermally induced phenomena including amorphisation, recrystallisation, contraction and melting.

Synthesis and thermal response of ZIF-61

To investigate the influence of different linker chemistry on the melting behaviour of **zni** topology ZIFs, ZIF-61 was studied. This framework exhibits the **zni** topology but contains

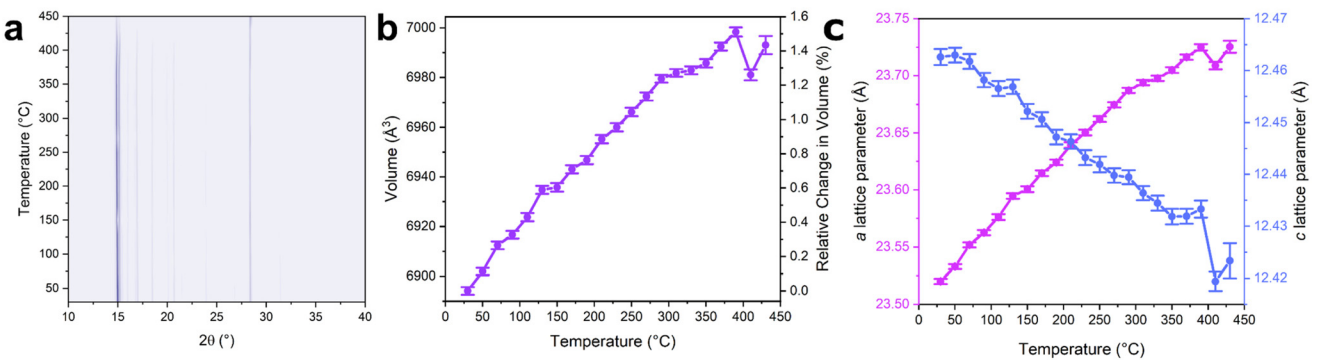

Fig. 3 Contour plot of diffraction data as a function of temperature for ZIF-zni (a). The high intensity reflection at *ca.* 28.5° 2θ is from the silicon standard. Change in unit cell volume (b) and lattice parameters (c) as a function of temperature. Volume parameters were extracted from Rietveld refinements of the diffraction data (Fig. S14–S17, Tables S2–S4†).

the 2-methylimidazolate linker.[54] Initial attempts of the synthesis based on previous reports, resulted in the formation of a mixed phase material exhibiting reflections corresponding to both ZIF-61 (**zni** topology) and ZIF-4 (**cag** topology) (Fig. S18†). Due to the reported thermodynamic stability of the **zni** topology,[45,56] the synthesis was optimised by increasing the reaction temperature to a minimum of 130 °C in order to force the crystallisation of only ZIF-61. This resulted in the formation of phase pure ZIF-61 as pale yellow rod-shaped crystals (Fig. S19–S22, Table S5†) with a composition of $[Zn(Im)_{1.35}(mIm)_{0.65}]$ (Fig. S23†).

The thermal response of ZIF-61 was then studied (Fig. 4, S24 and S25†). Unlike ZIF-zni, a defined mass loss of *ca.* 1.6% occurred below 400 °C (Fig. S24†). Thermal decomposition of ZIF-61 could then be separated into several stages beginning at 470 °C with *ca.* 3.5% mass lost in the first decomposition step (Fig. S24†). The 1st upscan of the DSC contained two noteworthy features: an exotherm (362 °C, −10 J g^{-1}) followed by a large endotherm with its onset at 564 °C that did not reach a maximum before the end of the scan at 590 °C (Fig. 4 and S25†). Upon reheating, no T_g was observed, and the DSC trace was relatively flat and featureless (Fig. 4 and S25†). This suggested that, unlike ZIF-zni, the endotherm at the end of the 1st upscan was not a melting event and was more likely due to sample decomposition. The presence of Bragg reflections corresponding to ZIF-61 in the sample after cooling from 590 °C (Fig. S26†), further support this. Moreover, a sample of ZIF-61 cooled from 590 °C displayed significant sample discolouration by optical microscopy (Fig. S27†) and defined crystalline facets were still evident from SEM (Fig. 4 and S28†). ^{1}H NMR of this heated sample revealed a significant reduction in mIm in the framework with an overall change in the proportion of Im to mIm to $[Zn(Im)_{1.82}(mIm)_{0.18}]$ (Fig. S29†). This supports that ZIF-61 does not undergo melting and instead decomposes at high temperatures, with decomposition initiating at the mIm linker.

To investigate this further, ZIF-61 was heated sequentially to 550 °C, 580 °C, 590 °C, 600 °C, 650 °C and 700 °C followed by *ex situ* PXRD (Fig. S30†). Reflections corresponding to ZIF-61 were seen as high as 600 °C, suggesting melting had not occurred at this stage. Peaks corresponding to zinc oxide were also visible at 600 °C. At 650 °C and 700 °C there was little evidence of diffuse scattering in the diffraction pattern, and the reflections corresponding to zinc oxide increased in intensity. These results support our hypothesis that ZIF-61 decomposes without undergoing melting.

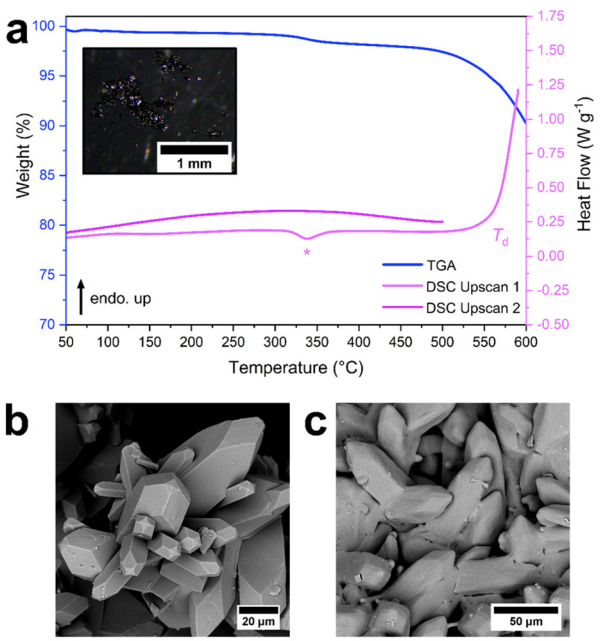

Fig. 4 (a) TGA trace (blue) and DSC traces (purple) of ZIF-61 revealing a decomposition endotherm with an onset at 564 °C (upscan 1) when heated to 590 °C and no evidence of T_g (upscan 2) when reheated to 500 °C, measured at 10 °C min^{-1} under argon. The exotherm at 362 °C in upscan 1 is marked by an asterisk. DSC upscan 2 is offset on the y axis for clarity. Inset: image of ZIF-61 after heating to 590 °C. SEM images of ZIF-61 (b) and ZIF-61 post 590 °C (c), scale bars are 20 μm and 50 μm respectively.

Further investigating the thermal response of ZIF-61

The exotherm at 362 °C in the DSC of ZIF-61 was then investigated. ZIF-61 was heated to 400 °C (*i.e.*, above the feature of interest), cooled to 30 °C, then re-heated to 400 °C (Fig. S31, S32†). Unlike ZIF-zni, the exotherm was only seen in the 1st upscan of the DSC, suggesting that the thermal event was irreversible. As the exotherm was accompanied by a 1.6% mass loss in the TGA trace (Fig. S24†), it was attributed to a small decomposition event, likely located at the mIm linker. Further evidence supporting this was a slight reduction of the mIm linker present in the structure $[Zn(Im)_{1.38}(mIm)_{0.62}]$ after heating to 400 °C (Fig. S33†) and a significant reduction in the intensity of the Bragg reflections of the diffraction pattern after holding at 365 °C for 1 hour (Fig. S34†). This was further confirmed by *in situ* VTPXRD (Fig. S35†) which revealed a significant reduction in the crystallinity of the sample above 250 °C. This correlated with both the exotherm seen in the DSC and the 1.6% mass loss event observed in the TGA, suggesting that ZIF-61 undergoes a small irreversible decomposition event below 400 °C and this is most likely located at the mIm linker.

The thermal decomposition of a ZIF containing the mIm linker has already been studied in detail.[57] In this work, Lin *et al.* studied the decomposition of ZIF-8 $[Zn(mIm)_2]$ under various atmospheric conditions. It was found that isothermal heat treatments at 300 °C resulted in significant carbonisation of the ZIF, regardless of the atmospheric conditions used.[57] This decomposition process was proposed to occur *via* degradation of a fraction of the mIm linkers to azirine rings.[57] We therefore hypothesise that, as ZIF-61 undergoes a defined mass loss in this temperature region, that a potentially similar decomposition mechanism occurs in this system. We also propose that this process occurs spontaneously, as the mass loss is accompanied by an exothermic event observed by DSC (Fig. 4 and S25†).

Comparison of the thermal behaviour of ZIF-zni and ZIF-61

Apart from the lower thermal stability of ZIF-61 compared to ZIF-zni below 400 °C, ZIF-61 also behaves differently at higher temperatures. ZIF-61 displayed a decomposition endotherm at 564 °C whereas ZIF-zni underwent melting with this event finishing at 576 °C. The differences in melting behaviour between ZIF-zni and ZIF-61 are attributed to the presence of the mIm linker in ZIF-61. The mIm linker is significantly bulkier than the Im linker, with steric indexes of 319 Å^4 and 248 Å^4, respectively.[58] Melting relies on the dissociation and reassociation of the organic linkers.[28] We hypothesise that the bulkier linker in ZIF-61 may hinder linker dissociation due to steric effects, resulting in a rise in its melting temperature above its decomposition temperature, *i.e.*, $T_m > T_d$. Steric effects are also likely to dominate in dense frameworks, such as those displaying the **zni** topology. It should also be noted that, in mixed-linker ZIFs, an uneven ligand distribution has been shown to influence the thermal response.[59] Therefore, the precise distribution of Im and mIm within ZIF-61 may also be influencing the thermal behaviour we observe here. The chemistry, and distribution, of the organic linkers therefore plays an important role in controlling melting in **zni** topology ZIFs.

Synthesis and thermal response of ZIF-zni-NH_2

Several studies have demonstrated that the thermal response and physical properties of ZIFs are highly sensitive to their chemical composition, and that judiciously controlling the quantity of a second organic linker can significantly alter their melting behaviour.[18,41] For example, reducing the bIm content in ZIF-62 by 10% was found to lower its T_m by 28 °C.[41] Furthermore, doping ZIF-4 with *ca.* 2.5% bIm significantly lowered its T_m by inhibiting its recrystallisation at high temperatures.[18] It has also recently been reported that post-synthetically modifying a ZIF resulted in a change in its surface water contact angle by over 30°, despite only a 1% change in its linker chemistry.[60] Here, we wanted to investigate the chemical sensitivity of melting in ZIFs further by achieving a level of chemical doping of less than 1%.

A synthesis of ZIF-zni was therefore attempted that would incorporate a very small quantity of a second linker into the structure. 5-aminobenzimidazolate (abIm – $C_7H_6N_3^-$) was chosen as the second linker as it was recently reported to significantly reduce the melting temperature in a **cag** topology ZIF.[60] Briefly, zinc nitrate hexahydrate, imidazole and 5-aminobenzimidazole were mixed in DEF before heating at 130 °C for 48 h (Fig. S36†). This resulted in the formation of red rod-shaped crystals (Fig. 5, S37 and S38†), with the strong colour of these crystals supporting the inclusion of abIm within the framework.[60] PXRD supported crystallisation in a **zni** topology framework, with a reasonable Pawley fit obtained using ZIF-zni as a starting model *i.e.*, using the $I4_1cd$ space group (Fig. S39, Table S6†). ^{1}H NMR spectroscopy was used to confirm the incorporation of abIm within the framework. The presence of a new singlet peak at 9.75 ppm supported the incorporation of the abIm linker, giving an overall composition of

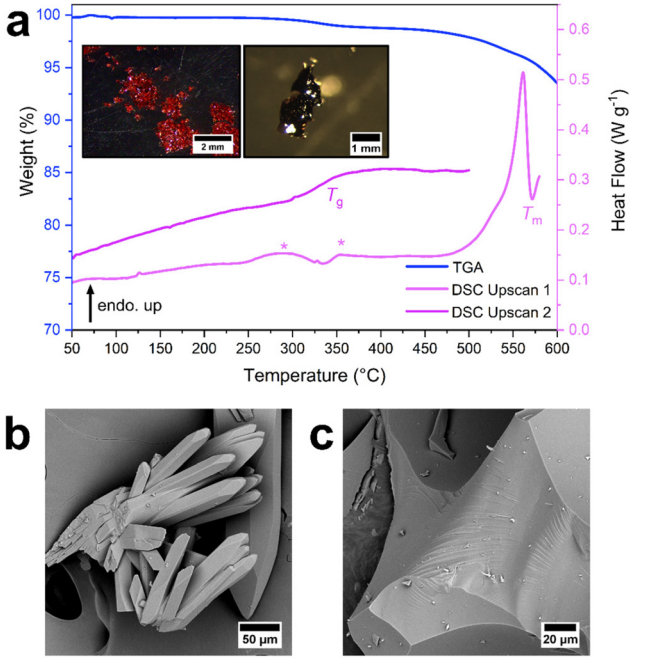

Fig. 5 (a) TGA trace (blue) and DSC traces (purple) of ZIF-zni-NH_2 revealing T_m = 569 °C (upscan 1) when heated to 580 °C and T_g = 343 °C (upscan 2) when reheated to 500 °C both at 10 °C min^{-1} under argon. Fluctuations at 291 °C and 354 °C in upscan 1 are marked by asterisks. DSC upscan 2 offset on the y axis for clarity. Insets: image of crystalline ZIF-zni-NH_2 illustrating bright red colour of crystals, and a fragment of a_gZIF-zni-NH_2, exhibiting evidence of particle amalgamation and flow. SEM images of ZIF-zni-NH_2 (b) and a_gZIF-zni-NH_2 (c), scale bars are 50 µm and 20 µm respectively.

$[Zn(Im)_{1.995}(abIm)_{0.005}]$ (Fig. S40†). The extremely low fraction of abIm in the framework (just 0.25%) is rationalised by the high crystallographic density of the **zni** topology framework limiting the space available for the inclusion of the abIm linker within the structure. To accommodate the sterically bulky abIm linker within the framework, it is likely that a small number of missing metal or missing linker defects are also present in the structure. However, the precise location of abIm within ZIF-zni-NH_2 and the resulting structural defects caused by its inclusion are beyond the scope of this study.

To confirm that abIm was incorporated into the ZIF, a sample was heated to 400 °C. Subsequent ^{1}H NMR spectroscopy revealed that the 9.75 ppm singlet of the abIm linker was still present (Fig. S41†), supporting its incorporation within the structure. This ZIF will be denoted ZIF-zni-NH_2 to highlight that a small quantity of abIm has been doped into the **zni** structure.

The thermal response of ZIF-zni-NH_2 was then studied (Fig. 5, S42 and S43†) to investigate how a subtle change in linker chemistry (just 0.25%) influenced its thermal response. Unlike pure ZIF-zni, a defined mass loss of *ca.* 1.1% occurred below 400 °C (Fig. S42†). The TGA trace was then relatively featureless until thermal decomposition began at 470 °C (Fig. S42†). Overall, the TGA trace was like those observed for ZIF-zni and ZIF-61 (both T_d = 470 °C), suggesting that doping

ZIF-zni with abIm has little influence upon its overall thermal stability.

The 1st upscan of the DSC contained small fluctuations in the heat flow trace between 250 °C and 400 °C (Fig. S43†) which correlated with the *ca.* 1.1% mass loss seen in the TGA (Fig. S42†). These are likely due to small decomposition events, potentially located around the abIm linker, in a similar fashion to ZIF-61. These fluctuations were followed by a sharp endotherm which was attributed to a melting event (T_m = 569 °C, 35.9 J g^{-1}) (Fig. 5, S43†). Furthermore, upon reheating, a T_g = 343 °C (Fig. 5 and S43†) was observed.

A sample of ZIF-zni-NH_2 cooled from 580 °C exhibited diffuse scattering by PXRD, supporting that melting and glass formation had occurred (Fig. S44†). Evidence of flow was also evident from both optical microscopy (Fig. S45†) and SEM (Fig. 5 and S46†), with flow-related striations visible in the latter images. After heating to 580 °C, ZIF-zni-NH_2 exhibited multiple new peaks in its ^{1}H NMR spectrum (Fig. S47†), suggesting that melting was accompanied by some linker decomposition. However, there was no evidence of zinc oxide in the diffraction pattern of ZIF-zni-NH_2 after heating to 580 °C—in stark contrast to ZIF-zni (Fig. S7 and S44†). This lack of zinc oxide was promising, suggesting that ZIF-zni-NH_2 is the first reported **zni** topology ZIF to melt and form a glass without zinc oxide formation. To confirm this, ZIF-zni-NH_2 was heated to 500 °C, 550 °C, 560 °C, 570 °C and 580 °C followed by *ex situ* PXRD (Fig. S48†). ZIF-zni-NH_2 retained its crystallinity to temperatures as high as 560 °C. However, above 570 °C, only diffuse scattering was observed with no evidence of zinc oxide by PXRD.

Discussion of the thermal response of ZIF-zni-NH_2

The melting event in ZIF-zni-NH_2 finished 7 °C lower (569 °C) than in ZIF-zni (576 °C). As the only appreciable difference between ZIF-zni and ZIF-zni-NH_2 is the small quantity of abIm within the latter structure, the lowering of T_m is attributed to the presence of the amine functionalised linker. We speculate that abIm lowers T_m here by weaking the Zn-N coordination bonds in the framework, *i.e.*, the enthalpic contribution to melting, in line with previous studies.[60] The amine functionality on abIm also has the potential to form hydrogen bonds during the melting process. These dispersive interactions may stabilise the uncoordinated linkers that form during melting, reducing the energy barrier to dissociation and hence lowering the melting temperature.[60]

It is also possible that any structural defects that have grown in ZIF-zni-NH_2 to accommodate the sterically bulky abIm linker may also be contributing to its lower T_m compared to ZIF-zni. Furthermore, the distribution of the linkers within ZIF-zni-NH_2 may also be contributing to its thermal response, as has been observed for other mixed-linker ZIFs.[59] Further studies investigating the distribution of abIm within ZIF-zni-NH_2 would be valuable for further understanding its thermal behaviour.

On first observation, the lower T_m of ZIF-zni-NH_2 compared to ZIF-zni may seem somewhat surprising in that a 0.25% change in linker composition can alter the melting temperature by as much as 7 °C. However, there have already been many reports detailing how changes in composition can have a significant impact on the response of ZIFs to temperature. For example, ZIFs doped with multiple linkers have been shown to exhibit lower T_ms due to enhanced framework disorder.[19] Doping ZIFs with Co^{2+} has also been shown to lower T_m as well as strongly altering the colour of the framework.[41,42] Another recent work illustrated that doping ZIF-4 with small quantities of bIm inhibited its transition to a closed-pore phase upon cooling.[61] Moreover, the same treatment can drastically lower the T_m of ZIF-4 by inhibiting its recrystallisation to ZIF-zni at high temperatures.[18] However, until now, this strategy has predominantly focused on altering the thermal response of **cag** topology ZIFs. Our results here suggest the broader applicability of this doping strategy to other ZIF topologies to enhance their melting behaviour. Furthermore, our results here highlight the sensitivity of melting in ZIFs to surprisingly subtle changes in composition.

Conclusions

In this work we studied the melting behaviour of ZIF-zni in detail before going on to investigate how changing linker chemistry influences melting in **zni** topology frameworks. ZIF-zni was found to melt and form a glass with T_m = 576 °C and T_g = 322 °C. However, it was not possible to prepare a_gZIF-zni without the growth of zinc oxide due to the high temperatures required to achieve melting. A reversible feature was also observed in the DSC of ZIF-zni at 361 °C and *in situ* VTPXRD was used to reveal a subtle contraction in the unit cell volume of ZIF-zni around this temperature which is attributed to a change in coordination at the zinc centres.

Incorporation of mIm led to the preparation of ZIF-61 which, unlike ZIF-zni, did not melt or form a glass and instead decomposed above 564 °C. The difference in glass forming ability between ZIF-zni and ZIF-61 is rationalised in terms of the steric bulk of the linkers, with the enhanced size of mIm disfavouring the linker dissociation and reassociation necessary for melting.

Doping ZIF-zni with a small quantity of abIm resulted in a ZIF denoted ZIF-zni-NH_2 with composition [Zn$(Im)_{1.995}(abIm)_{0.005}$]. This ZIF was found to melt with T_m = 569 °C, *i.e.*, at a lower temperature than pure ZIF-zni despite only a 0.25% change in its composition. Furthermore, no evidence of zinc oxide was found in the resulting glass. Typically, the melting behaviour of ZIFs is altered by much larger compositional changes (*cf.* a 10% change in bIm content results in a 28 °C change in T_m for ZIF-62).[41] Moreover, in the inorganic glass domain, the properties of silicate glasses are typically altered using dopant concentrations on the order of 10 mol%.[62–64] Our results here highlight the sensitivity of melting in ZIFs to very subtle changes in chemical composition. Doping ZIFs with a very small quantity of a second linker is therefore a promising strategy to change their thermal

behaviour, providing a promising route for further expanding the field of a_gMOFs.

Author contributions

A.M.B conceptualised the project. A.M.B. synthesised and characterised all samples. C.C.B collected the SEM data. G.I.L. collected the VTPXRD data and performed the Rietveld refinements. A.F.S., M.F.T., C.C.B. and G.I.L. contributed useful discussions. T.D.B. supervised the project and acquired funding. A.M.B. wrote the manuscript and all authors contributed to the final version.

Conflicts of interest

There are no conflicts to declare.

Acknowledgements

A.M.B. acknowledges the Royal Society for funding (RGF\EA \180092) and the Cambridge Trust for a Vice Chancellor's Award (304253100). M.F.T. thanks Corning Incorporated for PhD funding. A.F.S. acknowledges the EPSRC for a PhD studentship under the industrial CASE scheme along with Johnson Matthey PLC (JM11106). T.D.B. thanks the Royal Society for both a University Research Fellowship (URF\R\211013) and a research grant (RGS\R2\212221). T.D.B. also gratefully acknowledges the EPSRC (EP/R015481/1). T.D.B. also thanks the Leverhulme Trust for a Philip Leverhulme Prize and T.D.B. and C.C.B. also gratefully acknowledge funding by a Leverhulme Trust Research Project Grant (RPG-2020-005). We extend our thanks to Andrew Mason and Duncan Howe for collection of all ^{1}H NMR spectra at the Yusuf Hamied Department of Chemistry, University of Cambridge. We also acknowledge both Dr Chris Ashling and Dr Remo Widmer for useful discussions.

References

1 T. D. Bennett, A. K. Cheetham, A. H. Fuchs and F. X. Coudert, *Nat. Chem.*, 2016, **9**, 11–16.
2 Z. Fang, B. Bueken, D. E. De Vos and R. A. Fischer, *Angew. Chemie - Int. Ed.*, 2015, **54**, 7234–7254.
3 E. G. Meekel and A. L. Goodwin, *CrystEngComm*, 2021, **23**, 2915–2922.
4 S. Dissegna, K. Epp, W. R. Heinz, G. Kieslich and R. A. Fischer, *Adv. Mater.*, 2018, **30**, 1–23.
5 M. J. Cliffe, E. Castillo-Martínez, Y. Wu, J. Lee, A. C. Forse, F. C. N. Firth, P. Z. Moghadam, D. Fairen-Jimenez, M. W. Gaultois, J. A. Hill, O. V. Magdysyuk, B. Slater, A. L. Goodwin and C. P. Grey, *J. Am. Chem. Soc.*, 2017, **139**, 5397–5404.
6 N. Castel and F.-X. Coudert, *J. Phys. Chem. C*, 2022, **126**, 6905–6914.
7 C. Orellana-Tavra, E. F. Baxter, T. Tian, T. D. Bennett, N. K. H. Slater, A. K. Cheetham and D. Fairen-Jimenez, *Chem. Commun.*, 2015, **51**, 13878–13881.
8 K. W. Chapman, D. F. Sava, G. J. Halder, P. J. Chupas and T. M. Nenoff, *J. Am. Chem. Soc.*, 2011, **133**, 18583–18585.
9 X. Wu, H. Yue, Y. Zhang, X. Gao, X. Li, L. Wang, Y. Cao, M. Hou, H. An, L. Zhang, S. Li, J. Ma, H. Lin, Y. Fu, H. Gu, W. Lou, W. Wei, R. N. Zare and J. Ge, *Nat. Commun.*, 2019, **10**, 1–8.
10 R. S. K. Madsen, A. Qiao, J. Sen, I. Hung, K. Chen, Z. Gan, S. Sen and Y. Yue, *Science*, 2020, **367**, 1473–1476.
11 D. A. Keen, *Crystallogr. Rev.*, 2020, **26**, 141–199.
12 A. F. Sapnik, I. Bechis, S. M. Collins, D. N. Johnstone, G. Divitini, A. J. Smith, P. A. Chater, M. A. Addicoat, T. Johnson, D. A. Keen, K. E. Jelfs and T. D. Bennett, *Nat. Commun.*, 2021, **12**, 1–12.
13 K. W. Chapman, G. J. Halder and P. J. Chupas, *J. Am. Chem. Soc*, 2009, **131**, 17546–17547.
14 T. D. Bennett, P. Simoncic, S. A. Moggach, F. Gozzo, P. MacChi, D. A. Keen, J.-C. Tan and A. K. Cheetham, *Chem. Commun.*, 2011, **47**, 7983–7985.
15 T. D. Bennett, S. Cao, J. C. Tan, D. A. Keen, E. G. Bithell, P. J. Beldon, T. Friscic and A. K. Cheetham, *J. Am. Chem. Soc.*, 2011, **133**, 14546–14549.
16 S. Muratović, B. Karadeniz, T. Stolar, S. Lukin, I. Halasz, M. Herak, G. Mali, Y. Krupskaya, V. Kataev, D. Žilić and K. Užarević, *J. Mater. Chem. C*, 2020, **8**, 7132–7142.
17 T. D. Bennett, Y. Yue, P. Li, A. Qiao, H. Tao, N. G. Greaves, T. Richards, G. I. Lampronti, S. A. T. Redfern, F. Blanc, O. K. Farha, J. T. Hupp, A. K. Cheetham and D. A. Keen, *J. Am. Chem. Soc.*, 2016, **138**, 3484–3492.
18 L. Frentzel-Beyme, M. Kloß, P. Kolodzeiski, R. Pallach and S. Henke, *J. Am. Chem. Soc.*, 2019, **141**, 12362–12371.
19 A. M. Bumstead, M. F. Thorne and T. D. Bennett, *Faraday Discuss.*, 2021, **225**, 210–225.
20 N. Ma and S. Horike, *Chem. Rev.*, 2022, **122**, 4163–4203.
21 T. D. Bennett and S. Horike, *Nat. Rev. Mater.*, 2018, **3**, 431–440.
22 S. Horike, S. S. Nagarkar, T. Ogawa and S. Kitagawa, *Angew. Chemie - Int. Ed.*, 2019, 2–15.
23 S. Li, R. Limbach, L. Longley, A. A. Shirzadi, J. C. Walmsley, D. N. Johnstone, P. A. Midgley, L. Wondraczek and T. D. Bennett, *J. Am. Chem. Soc.*, 2019, **141**, 1027–1034.
24 P. G. Debenedetti and F. H. Stillinger, *Nature*, 2001, **410**, 259–267.
25 K. S. Park, Z. Ni, A. P. Cote, J. Y. Choi, R. Huang, F. J. Uribe-Romo, H. K. Chae, M. O'Keeffe and O. M. Yaghi, *Proc. Natl. Acad. Sci.*, 2006, **103**, 10186–10191.
26 A. Phan, C. J. Doonan, F. J. Uribe-romo, C. B. Knobler, M. O. Keeffe and O. M. Yaghi, *Acc. Chem. Res.*, 2010, **43**, 58–67.
27 Y. Tian, C. Cai, Y. Ji, X. You, S. Peng and G. Lee, *Angew. Chem., Int. Ed.*, 2002, **41**, 1384–1386.

28 R. Gaillac, P. Pullumbi, K. A. Beyer, K. Chapman, D. A. Keen, T. D. Bennett and F. X. Coudert, *Nat. Mater.*, 2017, **16**, 1149–1155.
29 R. Gaillac, P. Pullumbi and F. X. Coudert, *J. Phys. Chem. C*, 2018, **122**, 6730–6736.
30 K. Noh, J. Lee and J. Kim, *Isr. J. Chem.*, 2018, **58**, 1075–1088.
31 P. Z. Moghadam, A. Li, S. B. Wiggin, A. Tao, A. G. P. Maloney, P. A. Wood, S. C. Ward and D. Fairen-Jimenez, *Chem. Mater.*, 2017, **29**, 2618–2625.
32 I. A. Baburin, S. Leoni and G. Seifert, *J. Phys. Chem. B*, 2008, **112**, 9437–9443.
33 I. A. Baburin and S. Leoni, *J. Mater. Chem.*, 2012, **22**, 10152–10154.
34 I. A. Baburin, B. Assfour, G. Seifert and S. Leoni, *Dalton Trans.*, 2011, **40**, 3796.
35 M. Arhangelskis, A. D. Katsenis, N. Novendra, Z. Akimbekov, D. Gandrath, J. M. Marrett, G. Ayoub, A. J. Morris, O. K. Farha, T. Friščić and A. Navrotsky, *Chem. Mater.*, 2019, **31**, 3777–3783.
36 D. W. Lewis, A. R. Ruiz-Salvador, A. Gómez, L. M. Rodriguez-Albelo, F. X. Coudert, B. Slater, A. K. Cheetham and C. Mellot-Draznieks, *CrystEngComm*, 2009, **11**, 2272.
37 M. E. Schweinefuß, S. Springer, I. A. Baburin, T. Hikov, K. Huber, S. Leoni and M. Wiebcke, *Dalton Trans.*, 2014, **43**, 3528–3536.
38 I. Baburin, C. Schröder, M. Wiebcke and S. Leoni, *Z. Anorg. Allg. Chem.*, 2010, **636**, 2086–2086.
39 A. M. Bumstead, M. L. Ríos Gómez, M. F. Thorne, A. F. Sapnik, L. Longley, J. M. Tuffnell, D. S. Keeble, D. A. Keen and T. D. Bennett, *CrystEngComm*, 2020, **22**, 3627–3637.
40 R. S. K. Madsen, S. Sarkar, B. B. Iversen and Y. Yue, *Chem. Commun.*, 2022, **58**, 823–826.
41 M. F. Thorne, M. L. Ríos Gómez, A. M. Bumstead, S. Li and T. D. Bennett, *Green Chem.*, 2020, **22**, 2505–2512.
42 L. Frentzel-Beyme, M. Kloß, R. Pallach, S. Salamon, H. Moldenhauer, J. Landers, H. Wende, J. Debus and S. Henke, *J. Mater. Chem. A*, 2019, **7**, 985–990.
43 R. Lehnert and F. Seel, *Z. Anorg. Allg. Chem.*, 1980, **464**, 187–194.
44 L. Frentzel-Beyme, P. Kolodzeiski, J.-B. Weiß and S. Henke, *ChemRxiv*, 2021, DOI: **10.26434/chemrxiv-2021-lq308**.
45 R. Galvelis, B. Slater, A. K. Cheetham and C. Mellot-Draznieks, *CrystEngComm*, 2012, **14**, 374–378.
46 E. C. Spencer, R. J. Angel, N. L. Ross, B. E. Hanson and J. A. K. Howard, *J. Am. Chem. Soc.*, 2009, **131**, 4022–4026.
47 C. A. Schröder, I. A. Baburin, L. Van Wüllen, M. Wiebcke and S. Leoni, *CrystEngComm*, 2013, **15**, 4036–4040.
48 C. A. Schröder, S. Saha, K. Huber, S. Leoni and M. Wiebcke, *Z. Krist. Cryst. Mater.*, 2014, **229**, 807–822.
49 N. Kourkoumelis, in *ICDD Annual Spring Meetings*, ed. L. O'Neill, Cambridge University Press, Cambridge, 2013, pp. 137–148.
50 A. A. Coelho, *J. Appl. Crystallogr.*, 2018, **51**, 210–218.
51 W. M. Yim and R. J. Paff, *J. Appl. Phys.*, 1974, **45**, 1456–1457.
52 D. M. Schubert, M. Z. Visi and C. B. Knobler, *Main Gr. Chem.*, 2008, **7**, 311–322.
53 C. Zhou, M. Stepniewska, J. M. Sørensen, L. Scarpa, G. Magnacca, V. Boffa, T. D. Bennett and Y. Yue, *Microporous Mesoporous Mater.*, 2018, **265**, 57–62.
54 R. Banerjee, A. Phan, B. Wang, C. Knobler, H. Furukawa, M. O'Keeffe and O. M. Yaghi, *Science*, 2008, **319**, 939–943.
55 T. D. Bennett, A. L. Goodwin, M. T. Dove, D. A. Keen, M. G. Tucker, E. R. Barney, A. K. Soper, E. G. Bithell, J. C. Tan and A. K. Cheetham, *Phys. Rev. Lett.*, 2010, **104**, 11503.
56 I. A. Baburin, S. Leoni, B. Assfour, G. Seifert and S. Leoni, *J. Mater. Chem.*, 2012, **22**, 10152–10154.
57 J. B. James and Y. S. Lin, *J. Phys. Chem. C*, 2016, **120**, 14015–14026.
58 J. Yang, Y. B. Zhang, Q. Liu, C. A. Trickett, E. Gutiérrez-Puebla, M.Á Monge, H. Cong, A. Aldossary, H. Deng and O. M. Yaghi, *J. Am. Chem. Soc.*, 2017, **139**, 6448–6455.
59 V. Nozari, C. Calahoo, L. Longley, T. D. Bennett and L. Wondraczek, *J. Chem. Phys.*, 2020, **153**, 204501.
60 A. M. Bumstead, I. Pakamore, K. D. Richards, M. F. Thorne, S. S. Boyadjieva, L. N. McHugh, A. F. Sapnik, D. S. Keeble, D. A. Keen, R. C. Evans, R. S. Forgan and T. D. Bennett, *Chem. Mater.*, 2022, **34**, 2187–2196.
61 J. Song, R. Pallach, L. Frentzel-Beyme, P. Kolodzeiski, G. Kieslich, P. Vervoorts, C. L. Hobday and S. Henke, *Angew. Chem., Int. Ed.*, 2022, e202117565.
62 H. Jabraoui, E. M. Achhal, A. Hasnaoui, J. L. Garden, Y. Vaills and S. Ouaskit, *J. Non-Cryst. Solids*, 2016, **448**, 16–26.
63 A. Pedone, G. Malavasi, A. N. Cormack, U. Segre and M. C. Menziani, *Chem. Mater.*, 2007, **19**, 3144–3154.
64 H. Jabraoui, Y. Vaills, A. Hasnaoui, M. Badawi and S. Ouaskit, *J. Phys. Chem. B*, 2016, **120**, 13193–13205.